Intermetallic *hcp*-PtBi/*fcc*-Pt Core/Shell Nanoplates Enable Efficient Bifunctional Oxygen Reduction and Methanol Oxidation Electrocatalysis

Yingnan Qin[a,b#], Mingchuan Luo[a#], Yingjun Sun[a,b], Chunji Li[a], Bolong Huang[c], Yong Yang[a], Yingjie Li[a], Lei Wang[b] and Shaojun Guo[a,d,e*]*

[a] Department of Materials Science & Engineering, College of Engineering, Peking University, Beijing, 100871, China.

[b] College of Chemistry and Molecular Engineering, Qingdao University of Science and Technology, Qingdao 266042, China.

[c] Department of Applied Biology and Chemical Technology, The Hong Kong Polytechnic University, Hung Hom, Kowloon, Hong Kong SAR.

[d] BIC-ESAT, College of Engineering, Peking University, Beijing, 100871, China.

[e] Department of Energy and Resources Engineering, College of Engineering, Peking University, Beijing, 100871, China.

[#] *These authors contributed equally.*

Corresponding author: bolong.huang@polyu.edu.hk; guosj@pku.edu.cn

Abstract

Two dimensional (2D), ordered intermetallic and core/shell architectures are highly desirable structural features for promoting electrocatalysis on Pt-based nanocrystals in terms of activity, durability and cost. However, it is an extreme challenge to achieve all these features in single catalytic nanostructure currently. Herein, we report a new class of 2D nanoplate catalyst composed of intermetallic *hcp*-PtBi core and ultrathin *fcc*-Pt shell synthesized by a facile one-pot wet-chemical approach. The unique structural features of PtBi/Pt core/shell nanoplates make them exhibit the highest oxygen reduction reaction (ORR) activity in all the reported PtBi-based catalytic system, and 5 times more active than commercial Pt/C catalyst for ORR. The combination of cyclic voltammograms, x-ray photoelectron spectroscopy and density functional theory calculations reveals that a weaker oxygen adsorption energy on Pt shell from *hcp*-PtBi/*fcc*-Pt core/shell nanoplates relative to that on commercial Pt, deriving from the Bi-p empty band suppression at the core/shell interface, is the key in greatly

boosting ORR activity of PtBi nanocatalysts system. Thanks to the intermetallic phase and core/shell architecture, *hcp*-PtBi/*fcc*-Pt core/shell nanoplates show little loss in electrochemically active surface area and ORR activity during the accelerated durability test. They also show enhanced catalytic performance for the electro-oxidation of liquid fuels in both acid and alkaline electrolytes. This work sheds light on the rational design of new 2D core/shell nanostructured catalysts for enhancing fuel cells electrocatalysis.

Keywords: oxygen reduction reaction; PtBi; nanoplates; intermetallic; core/shell

1. Introduction

Polymer membrane electrolyte fuel cell (PEMFC) is an attractive energy conversion technology due to its high efficiency, high energy density and low environmental impact, which can potentially reduce our reliance on fossil fuels.[1-5] However, the practical adoption of this technology is greatly limited by the high cost and low efficiency of the state-of-the-art platinum-based electrocatalysts that are used to compensate the high overpotential mainly from the sluggish oxygen reduction reaction (ORR) at the cathode.[6] Although a vast amount of efforts have been devoted to addressing this challenge,[7-10] a large gap regarding the electrocatalysis remains currently. To bridge this gap, a more efficient Pt-based electrocatalyst is highly desirable, and is expected to possess the following advanced properties: high Pt utilization, enhanced activity and satisfied durability.[11-12]

In the past decade, dramatic enhancement in electrocatalytic performance has been realized by tuning the morphology and architecture of PtM (M represents other transition metals) alloyed nanocrystals.[13-17] On one hand, the morphology of a given nanocrystal directly impacts the exposed facets, mass transport and the interaction with carbon support, and thus governs the catalytic performance.[17] Compared with the conventional nanoparticulate catalyst, anisotropic structures are more interesting for electrocatalysis.[18-19] In particular, 2 dimensional (2D) nanosheets or nanoplates have drawn extensive attention due to their high ratio of high-coordination surface atoms that are beneficial to both the catalytic activity and long-term stability.[20] On the other hand, rationally arranging the atomic position of Pt and M enables further promotion in catalytic performance.[21-22] For example, constructing core/shell structure with a pure Pt shell and a M or PtM core has achieved good

electrocatalytic activity for ORR in the past decade normally due to the ligand and/or strain effects.[23-25] Meanwhile, the presence of Pt shell can protect the inner M from dissolution during the electrochemical operation, thus contributing to the long-term stability.[26] Previous studies also show the stability can be further promoted by constructing an intermetallic PtM core, in which the mobility of M is greatly reduced.[27-31] Together, it is highly desired to develop intermetallic Pt-based nanocatalysts with a 2D morphology and a core/shell architecture.

The well-established studies on PtBi alloy catalysts mainly focused on applications of methanol-tolerance or methanol/formic acid oxidation because the addition of Bi enabled high tolerance to CO poisoning.[32-35] Nevertheless, no report has shown significantly improved ORR activity on PtBi alloy catalysts over benchmark Pt/C, probably due to the lack of deliberate control/tuning in composition, morphology and architecture. Herein, we report the direct synthesis of a novel 2D nanoplate with a core/shell structure composed of an intermetallic *hcp*-PtBi core and an ultrathin *fcc*-Pt shell for fuel cells related electrocatalysis. The PtBi nanoplates with a thickness of around 4.5 nm were obtained from a facile wet-chemical approach. Strikingly, as-prepared PtBi nanoplates showed the highest ORR activity in all the reported PtBi-based catalyst system, which is over 5 times higher than the commercial Pt/C catalyst. DFT calculations suggest the reason for ORR activity enhancement of *hcp*-PtBi/*fcc*-Pt core/shell nanoplates is caused by that the presence of inner Bi-p empty band reduces the over-binding of Pt-O bond on the Pt shell. Intermetallic phase and core/shell architecture also enable the PtBi nanoplates exhibit extremely high durability. Furthermore, the PtBi/Pt core/shell nanoplates exhibit much enhanced catalytic performance towards the methanol oxidation reaction (MOR) relative to commercial Pt/C in both acid and alkaline electrolytes. This work emphasizes the importance of rational design and construction of promising electrocatalytic nanostructures for clean and renewable energy innovations.

2. Experimental section

2.1. Synthesis of PtBi nanoplates

In a typical synthesis of PtBi nanoplates, Pt(acac)$_2$, (10 mg), Bi(Ac)$_3$, (9.6 mg), L-ascorbic acid (35.6 mg), NH$_4$Br, (50 mg), and a mixture of 1-octadecene and oleylamine (5 mL, v:v = 1:1) were added into a 25 mL flask. Afterwards, the flask was capped and sonicated for 1 h to obtain a clear homogeneous solution. Then, the flask was heated to 160°C in 30 min with a heating mantle, and kept

at 160 °C for 5 h. After cooling to room temperature, the colloidal products were collected by centrifugation, washed with cyclohexane for three times and dispersed in cyclohexane for further use.

2.2. Characterization

The TEM samples were prepared by dropping cyclohexane dispersed product onto carbon-coated copper transmission electron microscopy (TEM) grids using pipettes and dried under ambient condition. Low-magnification TEM was conducted on a FEI Tecnai-G2 T20. High-magnification transmission electron microscope (HRTEM) was conducted on a FEI Tecnai-G2 F30 at an accelerating voltage of 300 KV. XRD was conducted on an X'Pert-Pro X-ray powder diffractometer equipped with a Cu radiation source ($\lambda = 0.15406$ nm). The valence state of Pt and Bi element was conducted by an X-ray photoelectron spectroscopy (XPS) (AXIS supra/ultra Kratos Analytical Ltd.). The elemental composition and concentration of PtBi/C catalyst were determined by the inductively coupled plasma mass spectrometer (Agilent SureCycler 8800 Gradient Cycler).

2.3. Electrochemical measurements

Before electrochemical tests, the as-prepared PtBi nanoplates were deposited onto carbon black (EC-300) to obtain PtBi nanoplates/C catalyst. The catalyst powder was then dispersed and sonicated in a mixture containing isopropanol, water and Nafion solution (v: v: v = 1: 1: 0.016) to form a homogeneous catalyst ink, which was then quantitatively loaded onto a rotating disk glassy carbon electrode (RDE, diameter: 5 mm, area: 0.196 cm^2) to prepare the thin film work electrode. The Pt loading for each catalyst was around 10 μg/cm$^2_{geo}$. All electrochemical tests were conducted in a three-electrode system, with the catalyst coated RDE as the working electrode, Ag/AgCl electrode as the reference electrode and Pt foil as the counter electrode, respectively. Cyclic voltammograms (CVs) were conducted in N$_2$-saturated 0.1 M HClO$_4$ solution at a rate of 50 mV/s. The ORR polarization curves were recorded in O2-saturated 0.1 M HClO$_4$ at a scan rate and a rotation rate of 20 mV/s and 1600 rpm, respectively. The current densities in the ORR polarization curve were normalized in reference to the geometric area of the glassy carbon RDE (0.196 cm^2). The stability tests were performed at 0.1 M HClO$_4$ solution at room temperature by applying the cyclic potential sweep between 0.6 and 1.0 V versus RHE at a sweep rate of 100 mV/s for 5000 cycles.

3. Results and Discussion

The PtBi/Pt core/shell nanoplates were directly synthesized by heating a mixture of platinum (II) acetylacetone (Pt(acac)$_2$), bismuth (III) acetate (BiAc$_3$), ammonium bromide (NH$_4$Br), ascorbic acid, oleylamine and 1-octadecene in a flask at a temperature of 160 °C for 5 h. The resultant black colloid product was collected by centrifugation and washed with the mixture of cyclohexane/ethanol for

several times before being dispersed in cyclohexane for further use. Powder X-ray diffraction (PXRD) was used to characterize the crystalline phase of as-obtained PtBi/Pt core/shell nanoplates. As shown in **Figure. 1a**, the diffraction peaks at 29°, 41° and 42° can be indexed to the (101), (102), (110) planes of intermetallic *hcp*-PtBi, indicating a NiAs-type structure (P6₃/mmc). The morphology and composition of the as-prepared PtBi/Pt core/shell nanoplates were characterized by the means of transmission electron microscope (TEM) (**Figure 1b and 1c**), high-angle annular dark-field scanning TEM (HAADF-STEM) and energy dispersive X-ray spectroscopy (EDX). TEM image shows the majority of products are 2D nanoplates with either hexagonal or triangle shape. The EDX result reveals the Pt/Bi ratio of intermetallic PtBi/Pt core/shell nanoplate is around 66/34 (**Figure. 1d**), in accordance with the result from Inductively Coupled Plasma-Atomic Emission Spectrometry (ICP-AES). The average thickness of PtBi/Pt core/shell nanoplates is 4.6 nm, determined from the statistic of 20 stacks that lies vertically on the TEM grids (**Figure. 1e, f and Figure. S1**). STEM-EDX elemental mapping analysis demonstrates the homogeneous distribution of both Pt and Bi throughout the nanoplate (**Figure. 1g**), further confirming the intermetallic structure. X-ray photoelectron spectroscopy (XPS) confirms the presence of both Pt and Bi in the obtained nanoplate (**Figure. 1h and Figure. S2**). The majority of surface Pt is in metallic state as observed from the Pt 4f XPS spectra, while the majority of Bi takes the oxidation state. Furthermore, the Pt 4f peak of PtBi/Pt core/shell nanoplates shifts to the high binding energy by around 0.2 eV, indicating the electron transfer between Pt and Bi.[36]

High resolution TEM (HRTEM) image further reveals the crystalline nature of the product. As shown in **Figure. 2a and 2b**, a grain boundary can be readily identified along the edge, confirming the core/shell structure of as-obtained PtBi nanoplates. The thickness of the shell is around 1.0 nm, corresponding to nearly 4 atomic layers. The lattice spacing of the inner region is around 0.35 nm, being close to that of the (101) plane of *hcp*-PtBi, and in agreement with the XRD results.[13a] However, the interplanar spacing of edge region is determined to be 0.22 nm, suggesting the typical (111) plane of *fcc*-Pt in the shell. The core/shell structure was further verified by EDX spectroscopy line-scan profiles of single PtBi nanoplate (**Figure. 2c and 2d**). Based on the above observation, we conclude the as-obtained nanoplate is composed of an intermetallic *hcp*-PtBi core and a *fcc*-Pt shell.

To shed light on the growth mechanism for 2D PtBi/Pt core/shell nanoplates, we traced the morphological evolution by characterizing the product collected at different stages. **Figure. 3a** shows the TEM image of products collected at the moment when the reaction solution just turned black, representing a typical phenomenon of burst nucleation stage of nanocrystals.[37] The majority of products were nanoclusters with an average size of 2.5 nm, which served as the nuclei for further

growth. After the temperature reached 160 °C for a period of 5 min, a mixture of ill-defined nanoplates and nanoparticles were obtained. During this period, the average size of product rapidly increased to 9.5 nm (**Figure. 3b**). For the next 5 h, the nanoparticles gradually diminished, giving rise to highly pure and uniform nanoplates with a hexagonal shape and a lateral size of 29 nm (**Figure. 3c**). However, if the reaction time was prolonged to 10 h, the lateral size of products further increased to 35.3 nm with a much wider size distribution relative to that of products at 5 h, even though the 2D morphology could be well maintained (**Figure. 3d**). This phenomenon is probably due to the Ostwald ripening, where the smaller nanocrystals gradually dissolved into the solution and then re-deposited onto the surface of larger nanocrystals to lower the surface free energy.[38] The overall structural evolution of PtBi/Pt core/shell nanoplates is illustrated in **Figure. 3e**.

The wet-chemical synthesis of anisotropic nanocrystal with high aspect ratio is very challenging due to the inherently thermodynamic instability of anisotropic morphologies, such as 1D nanowires or nanotubes, 2D nanoplates or nanosheets.[39] It is well established that the resultant morphology of nanocrystal is governed by the kinetics of nucleation and growth, which experimentally depends on the choice and concentration of reducing agents, the solvent, the capping agents and other structure-directing agents.[40] To investigate the key experimental parameters for the formation of 2D PtBi/Pt core/shell nanoplates, a series of control experiments have been carried out. We found the bromide ions were essential to the yield of uniform nanoplates, because only irregular products could be obtained in the absence of NH_4Br (**Figure. S4**). Additionally, PtBi nanoplates could also be obtained by replacing NH_4Br with other bromide ions suppliers, such as CTAB (**Figure. S5**). It has been reported that the halide ions could selectively adsorb on distinct surfaces of nanocrystals and guide the anisotropic growth, thus resulting in different morphologies.[41] We then replaced Br^- with Cl^- and I^- to investigate if other halide ions had the same structural-directing effects. However, even though 2D nanoplates could also be obtained in these cases, the products were severely aggregated with non-uniform size and morphology (**Figure. S6**). These control experiments highlight the essential role of bromide ion in the synthesis of 2D nanoplates in our system.

In addition to bromide ion, CO molecules were also widely used as capping agents to guide the growth of 2D metallic nanocrystals.[42]. However, when $Mo(CO)_6$ was used as the CO supplier in our synthetic system, only PtBi nanocubes could be obtained (**Figure. S7**). Besides, the morphology of

products also depended on the choice of solvent, as no nanoplates could be obtained if pure oleylamine was used as the solvent (**Figure. S8**). We also investigated the influence of reducing agents on the final morphology of products, and found: (1) a lower or higher concentration of AA than the optimized value could lead to nanoplates with inhomogeneous size distribution (**Figure. S9**); (2) the use of glucose as reducing agent could also produce nanoplates (**Figure. S10**), whereas the use of a weak reducing agent, such as phenylamine, could only yield irregular products (**Figure. S11**). As shown in **Figure S12**, the feeding ratio of Pt/Bi precursors played the dominant role in determining the final products. Increasing the Pt/Bi ratio from 1/1 to 2/1 resulted in an obvious increase in the shell thickness, while decreasing the Pt/Bi ratio to 1/2 resulted in a homogeneous nanoplate in the absence of core/shell structure, further implying that the shell was made of pure Pt.

To study the electrocatalytic properties of PtBi/Pt core/shell nanoplates, we first deposited the freestanding nanoplates onto commercial carbon black (C, EC-300) by sonication to obtain carbon supported catalyst (denoted as PtBi nanoplates/C). The as-obtained PtBi nanoplates/C was then subjecting to annealing at 220 for 1 h to remove the excess OAm before being used to prepare the catalysts ink. TEM images show that the PtBi nanoplates were uniformly dispersed on the carbon support without changes in their original morphology after this treatment (**Figure. S13c**). For a comparison, the commercial Pt/C (Jonhson-Matthey Corp.) (**Figure. S13a**) was used as benchmark. Cyclic voltammetries (CVs) were first conducted to reveal the surface property of as-obtained catalyst. As shown in **Figure. 4a**, the PtBi nanoplates/C displayed typical Pt signals: well-defined hydrogen adsorption/desorption region (0.05 to 0.4 V *versus* RHE) and redox Pt oxidation/reduction region (0.7 to 1.1 V *versus* RHE), again suggesting the exposed surface of PtBi nanoplates are pure Pt.[43] Notably, the on-set potential for oxidation peak, corresponding to the commencement of hydroxyl adsorption, shifted positively by more than 100 mV in comparison with that of commercial Pt/C, indicating a weaker oxygen binding energy on the surface of PtBi nanoplates.[44] According to the Sabatier principle, slightly weakening the Pt-O strength could shift the oxygen binding energy of Pt to the optimized value (the peak position of volcano plot), thus leading to enhanced ORR activity. The hydrogen desorption peak in the recorded CV was applied to calculate the electrochemically active surface area (ECSA) of each catalyst. As listed in **Table S1**, the ECSA of PtBi nanoplates/C was 33.9 m^2/g, which is smaller than that of commercial Pt/C owing to a larger dimensional size.

Figure. 4b compares the ORR polarization curves of various catalysts in O_2-saturated 0.1 M $HClO_4$ solution. In comparison with Pt/C, a positive shift in the half-wave potential ($E_{1/2}$) can be readily identified on PtBi nanoplates/C, indicating its fast kinetics for the electro-reduction of oxygen. To provide a quantitative and fundamental comparison on intrinsic activity, it is routinely to obtain specific activity (SA) at 0.9 V *versus* RHE by calculating the kinetic current (i_k) *via* the Koutechy-Levich equation and then normalizing i_k to the specific surface area. Similarly, mass activity (MA) was obtained by normalizing i_k to the Pt mass. As shown in **Figure. 4c**, the SA of PtBi nanoplates/C reaches 1.04 mA/cm_{Pt}^{-2}, which is 5.2 times higher than that of Pt/C. Meanwhile, even with a smaller ECSA, the mass activity of PtBi nanoplates/C was more than 2 times higher than that of Pt/C. Impressively, the PtBi nanoplates/C also exhibits enhanced durability relative to Pt/C. As compared in **Figure. 4d**, after a course of 5,000 potential cycles, the PtBi nanoplates/C still maintains more than 90 % of the initial ECSA, much higher than that of Pt/C. The loss of ECSA for Pt/C is mainly caused by the growth and aggregation of active components, which can be verified from the TEM of catalysts before and after durability tests (**Figure. S13d**). TEM-EDX of PtBi nanoplates/C after durability test shows that a small amount of Bi has been lost during cycling, which might be responsible for the slight decrease in specific activity (**Figure. 4d and Figure S13e**). Both the intermetallic phase and the Pt shell can minimize the mobility and dissolution of non-stable Bi atoms, thus contributing to the enhanced long-term durability.

It is well-known that an optimum oxygen adsorption energy (OAE) is essential to the ORR activity, which can be reflected by the position of d-band centre.[45-46] We then carried out density functional theory (DFT) calculations to shed light on the impressive ORR activity of PtBi nanoplates/C. The flat slab interface structural model has been built between *hcp*-PtBi (*P63/mmc*) and *fcc*-Pt with four-layered thickness. The final relaxed structure shows the interface has been well formed by the flexibly arranged local Pt-Bi bonding structure. The local lattice of the *fcc*-Pt shows a slight distortion. The electronic bonding (filled-states) and anti-bonding (empty states) orbitals have both been shown (**Figure 5a**). There are three main peaks for the broadened Pt-5d band near Fermi level (E_F), which indicates three different activities bonding and charge transfer found in this interface system. The Bi-p bands cross the E_F denotes potentially high electronic activities to overlap similarly high-lying s-bands (**Figure 5b**). The variations of the d-band center for the Pt-5d orbital within different regions of interface have

been illustrated. The introduction of electronically active Bi-p orbital suppresses the Pt-5d band centers (**Figure 5c**). From the *fcc*-Pt bulk to the surface Pt-site from *hcp*-PtBi alloy, the band center has been downshifted about 1.8 eV. The over-binding effect of Pt site has shown to be ameliorated. However, too weak bonding does not possess a favorable initial adsorption. We further notice that the Pt-site at the interface has moderately suppressed the band center with about 0.9 eV shifting. This indicates the energy evolution pathway can be favorably driven by different local Pt contributions.

The pathways for acidic four-electron ORR based on PtBi-Pt and PtBi systems have been shown, respectively (**Figure 5d**). Overall, the PtBi-Pt (-4.69 eV) is more energetic favorable than PtBi (-3.00 eV) to generate $2H_2O$. The initial adsorption of $*O_2$ and $4H*$ demonstrates more energetic preferences in PtBi-Pt (-1.78 eV) compared to PtBi (-0.80 eV), which is a rate determining step (RDS). However, for PtBi system, too strong in-plane Bi-(p) and O-(p) or H-(s) overlapping leads to over-binding effect of $*O=O-H$ and adsorbing H^+. This yields an energetic barrier of 1.02 eV to form $*O+H_2O+2(H^++e^-)$. Another barrier (1.35 eV) is found from $*OH+(H^++e^-)$ to H_2O, which arises because of strong overlapping between Bi-(p) and H-(s). Finally, a clear contrast is shown for the product H_2O formation, which is energetically downhill for PtBi-Pt and uphill for PtBi, respectively. From the local structures (**Figure 5e**), the O-related intermediate molecules are simultaneously bonding with Bi and Pt sites at the interface, where has higher catalytic activities. Therefore, in the PtBi-Pt interface system, the Bi suppresses the Pt-(H, O) overbinding effect, and the efficiency of adsorption/desorption steps have been increased with barrier free.

The electrocatalytic properties of PtBi nanoplates/C towards the MOR was evaluated by conducting CVs in 0.1 M $HClO_4$ containing 0.1 M methanol. Obviously, the recorded peak current corresponding to the oxidation of methanol of PtBi nanoplates/C was far higher than that of commercial Pt/C (**Figure 6a and 6b**). The specific and mass activities were obtained by normalizing the peak current to the specific area and mass of Pt, respectively. As shown in **Figure 6c**, the specific and mass activities of PtBi nanoplates/C reach 3.18 mA/cm^2 and 1.1 A/mg, 7.4 and 3.7 times higher than those of Pt/C, respectively. The electrochemical stability was assessed by recording i-t curves at a constant potential of 0.67 V *versus* RHE. After a course of 4000 s, the MOR current of PtBi nanoplates/C was still higher than that of Pt/C, indicating its good durability (**Figure 6d**). We also evaluated the catalytic performance of MOR in alkaline electrolyte, conducted in identical conditions

with that of acidic electrolyte except changing the electrolyte to 0.1 M KOH containing 0.1 M MeOH. As expected, the PtBi nanoplates/C also shows higher activity and better durability than commercial Pt/C (**Figure S15**).

4. Conclusions

In conclusion, we demonstrate a new class of intermetallic *hcp*-PtBi/*fcc*-Pt core/shell nanoplates for promoting fuel cells related electrocatalysis. The PtBi nanoplate shows bi-functionalities and outperforms commercial Pt/C not only in the electro-reduction of oxygen, but also in the electro-oxidation of liquid fuels. DFT calculations reveals that the enhanced ORR electrocatalysis stems from the fact the presence of Bi-p empty bands can reduce the over-binding effect of Pt-O on Pt shell of *hcp*-PtBi/*fcc*-Pt core/shell nanoplates. The *hcp*-PtBi/*fcc*-Pt core/shell nanoplates are stable for ORR by reflecting negligible loss in electrochemically active surface area and activity after the accelerated durability test due to their interesting intermetallic phase and core/shell architecture. Even higher mass activity of this catalytic system can be envisioned by further decreasing the thickness of nanoplates and the *fcc*-Pt shell. This study presents a new catalytic structure with excellent activity and durability, and also emphasizes the importance of rational structural design and construction of electrocatalysts with excellent performance.

AUTHOR INFORMATION
Corresponding Authors
* E-mail: bolong.huang@polyu.edu.hk.
* E-mail: guosj@pku.edu.cn.
Notes
The authors declare no competing financial interest.

Supporting Information

The Supporting Information is available free of charge on the ACS Publications website at DOI:

Details of the experiments and Tables S1−S3 and Figures S1−S15 as described in the text. (PDF)

References

(1) Debe, M. K. *Nature* **2012**, *486*, 43-51.

(2) Mazumder,V.; Lee, Y.; Sun, S. *Adv. Funct. Mater.* **2010**, *20*, 1224-1231.

(3) Gasteiger, H. A.; Kocha, S. S.; Sompalli, B.; Wagner, F. T. *Appl. Catal. B: Environ.* **2005**, *56*, 9-35.

(4) Oezaslan, M.; Hasché, F.; Strasser, P. *J. Phys. Chem. Lett.* **2013**, *4*, 3273-3291.

(5) Gröger, O.; Gasteiger, H. A.; Suchsland, J. –P. *J. Electrochem. Soc.* **2015**, *162*, A2605-A2622.

(6) Seh, Z. W.; Kibsgaard, J.; Dickens, C. F.; Chorkendorff, I.; Norskov, J. K.; Jaramillo, T. F. *Science* **2017**, *355*, eaad4998.

(7) Luo, M.; Sun, Y.; Wang, L.; Guo, S. *Adv. Energy Mater.* **2017**, *7*, 1602073.

(8) Strasser, P.; Kühl, S. *Nano Energy* **2016**, *29*, 166-177.

(9) Wang, Y.; Zhao, N.; Fang, B.; Li, H.; Bi, X.; Wang, H. *Chem. Rev.* **2015**, *115*, 3433-3467.

(10) Guo, S.; Zhang, S.; Sun, S. *Angew. Chem. Int. Ed.* **2013**, *52*, 8526-8544.

(11) Jiao, Y.; Zheng, Y.; Jaroniec, M.; Qiao, S. *Chem. Soc. Rev.* **2015**, *44*, 2060-2086.

(12) Wu, J.; Yang, H. *Acc. Chem. Res.* **2013**, *46*, 1848-1857.

(13) Li, M.; Zhao, Z.; Cheng, T.; Fortunelli, A.; Chen, C.; Yu, R.; Zhang, Q.; Gu, L.; Merinov, B. V.; Lin, Z.; Zhu, E.; Yu, T.; Jia, Q.; Guo, J.; Zhang, L.; Goddard, W. A.; Huang, Y.; Duan, X. *Science* **2016**, *354*, 1414-1419.

(14) Escudero-Escribano, M.; Malacrida, P.; Hansen, M. H.; Vej-Hansen, U. G.; Velazquez-Palenzuela, A.; Tripkovic, V.; Schiotz, J.; Rossmeisl, J.; Stephens, I. E.; Chorkendorff, I. *Science* **2016**, *352*, 73-76.

(15) Bu, L.; Zhang, N.; Guo, S.; Zhang, X.; Li, J.; Yao, J.; Wu, T.; Lu, G.; Ma, J.; Su, D.; Huang, X. *Science* **2016**, *354*, 1410-1414.

(16) Zhang, L.; Roling, L. T.; Wang, X.; Vara, M.; Chi, M.; Liu, J.; Choi, S. I.; Park, J.; Herron, J. A.; Xie, Z.; Mavrikakis, M.; Xia, Y. *Science* **2015**, *349*, 412-416.

(17) Wang, C.; Daimon, H.; Onodera, T.; Koda, T.; Sun, S. *Angew. Chem. Int. Ed. Engl.* **2008**, *47* , 3588-3591.

(18) Bu, L.; Ding, J.; Guo, S.; Zhang, X.; Su, D.; Zhu, X.; Yao, J.; Guo, J.; Lu, G.; Huang, X. *Adv. Mater.* **2015**, *27*, 7204-7212.

(19) Jiang, K.; Zhao, D.; Guo, S,; Zhang, X.; Zhu, X.; Guo, J.; Lu, G.; Huang, X. *Sci. Adv.* **2017**, *3*, e1601705.

(20) Lopes, P. P.; Strmcnik, D.; Tripkovic, D.; Connell, J. G.; Stamenkovic, V. R.; Markovic, N. M. *Acs Catal.* **2016**, *6*, 2536-2544.

(21) Stamenkovic, V. R.; Mun, B. S.; Mayrhofer, K. J.; Ross, P. N.; Markovic, N. M. *J. Am. Chem. Soc.* **2006**, *128*, 8813-8819.

(22) Stamenkovic, V. R.; Mun, B. S.; Arenz, M.; Mayrhofer, K. J.; Lucas, C. A.; Wang, G.; Ross, P. N.; Markovic, N. M. *Nat. Mater.* **2007**, *6*, 241-247.

(23) Luo, M.; Wei, L.; Wang, F.; Han, K.; Zhu, H. *J. Power Sources* **2014**, *270*, 34-41.

(24) Yang, H. *Angew. Chem. Int. Ed. Engl.* **2011**, *50*, 2674-2676.

(25) Luo, M.; Guo, S. *Nat. Rev. Mater.* **2017**, *2*, 17059.

(26) Gan, L.; Cui, C.; Rudi, S.; Strasser, P. *Top. Catal.* **2013**, *57*, 236-244.

(27) Chung, D.; Jun, S.; Yoon, G.; Kwon, S. G.; Shin, D. Y.; Seo, P.; Yoo, J. M.; Shin, H.; Chung, Y.; Kim, H.; Mun, B. S.; Lee, K. S.; Lee, N. S.; Yoo, S. J.; Lim, D. H.; Kang, K.; Sung, Y. E.; Hyeon, T. *J. Am. Chem. Soc.* **2015**, *137*, 15478-15485.

(28) Kim, J.; Lee, Y.; Sun, S. *J. Am. Chem. Soc.* **2010**, *132*, 4996-4997.

(29) Kuttiyiel, K. A.; Sasaki, K.; Su, D.; LWu, L.; Zhu, Y.; Adzic, R. R. *Nat. Commun.* **2014**, *5*, 5185.

(30) Li, Q.; Wu, L.; Wu, G.; Su, D.; Lv, H.; Zhang, S.; Zhu, W.; Casimir, A.; Zhu, H.; Mendoza-Garcia, A.; Sun, S. *Nano Lett.* **2015**, *15*, 2468-2473.

(31) Wang, D.; Xin, H.; Hovden, R.; Wang, H.; Yu, Y.; Muller, D. A.; DiSalvo, F. J.; Abruna, H. D. *Nat. Mater.* **2013**, *12*, 81.

(32) Liao, H.; Zhu, J.; Hou, Y. *Nanoscale* **2014**, *6*, 1049-1055.

(33) Bauskar, A. S.; Rice, C. A. *Electrochim. Acta* **2013**, *93*, 152-157.

(34) Chen, Q.; Zhou, Z.; Vidal-Iglesias, F. J.; Solla-Gullon, J.; Feliu, J. M.; Sun, S. *J. Am. Chem. Soc.* **2011**, *133*, 12930-12933.

(35) Zhang, D.; Wu, F.; Peng, M.; Wang, X.; Xia, G.; Guo, G. *J. Am. Chem. Soc.* **2015**, *137*, 6263-6269.

(36) Mukerjee, S.; Srinivasan, S. *J. Electroanal. Chem.* **1993**, *357*, 201-224.

(37) Xia, Y.; Xiong, Y.; Lim, B.; Skrabalak, S. E. *Angew. Chem. Int. Ed.* **2009**, *48*, 60-103.

(38) Kwon, S. G.; Hyeon, T. *Small* **2011**, *7*, 2685-2702.

(39) Gilroy, K. D.; Ruditskiy, A.; Peng, H.; Qin, D.; Xia, Y. *Chem. Rev.* **2016**, *116*, 10414-10472.

(40) Wu, L.; Mendoza-Garcia, A.; Li, Q.; Sun, S. *Chem. Rev.* **2016**, *116,* 10473-10512.

(41) Wang, Y.; Peng, H.; Liu, J.; Huang, C.; Xia, Y. *Nano Lett.* **2015**, *15*, 1445-1450.

(42) Huang, X.; Tang, S.; Mu, X.; Dai, Y.; Chen, G.; Zhou, Z.; Ruan, F.; Yang, Z.; Zheng, N. *Nat. Nanotechnol.* **2011**, *6*, 28-32.

(43) Zhu, H.; Luo, M.; Zhang, S.; Wei, L.; F. Wang, F.; Wang, Z.; Wei, Y.; Han, K. *Int. J. Hydrogen Energy* **2013**, *38*, 3323-3329.

(44) Stamenkovic, V. R.; Fowler, B.; Mun, B. S.; Wang, G.; Ross, P. N.; Lucas, C. A.; Markovic, N. M. *Science* **2007**, *315*, 493-497.

(45) Nørskov, J. K.; Rossmeisl, J.; Logadottir, A.; Lindqvist, L.; Kitchin, J. R.; Bligaard, T.; Jónsson, H. *J. Phys. Chem. B* **2004**, *108*, 17886-17892.

(46) Stamenkovic, V.; Mun, B. S.; Mayrhofer, K. J.; Ross, P. N.; Markovic, N. M.; Rossmeisl, J.; Greeley, J.; Norskov, J. K. *Angew. Chem. Int. Ed.* **2006**, *45*, 2897-2901.
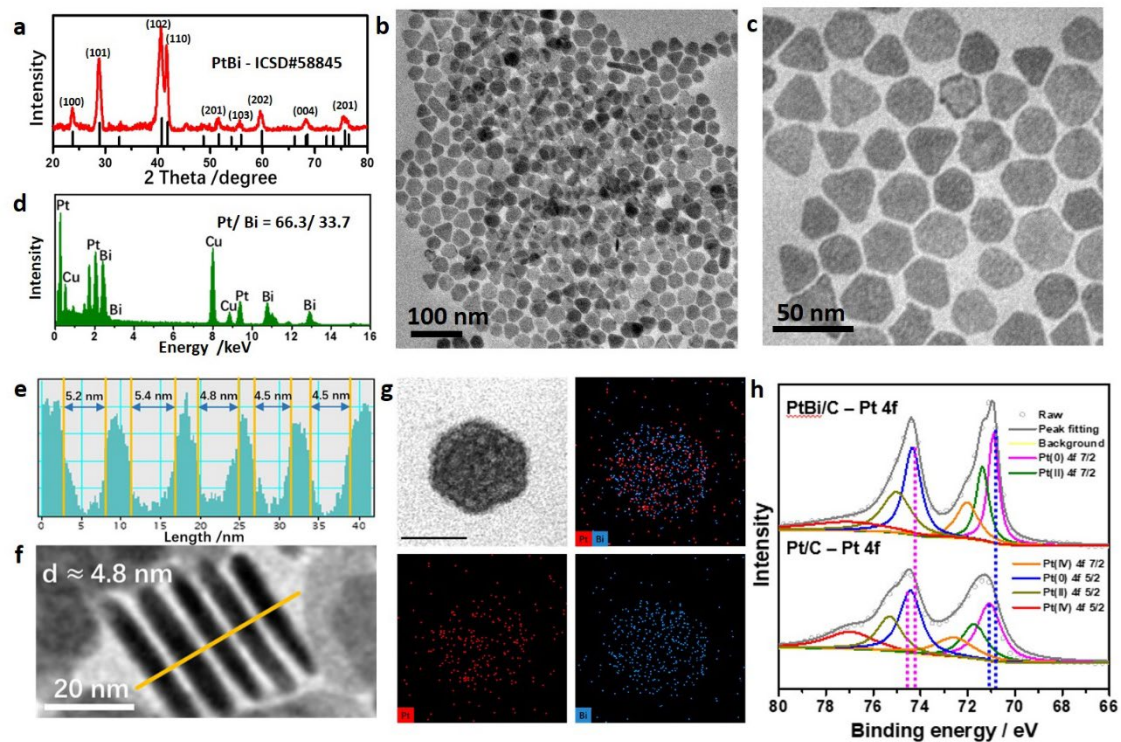
Figure 1 Morphology and structure characterization of PtBi/Pt core/shell nanoplates. (**a**) PXRD pattern, (b, c) TEM image, and (d) EDX of PtBi/Pt core/shell nanoplates. (**e, f**) TEM of PtBi/Pt core/shell stacks that lie vertically on the TEM grid and the corresponding thickness estimation. (**g**) STEM elemental mappings of single PtBi/Pt core/shell nanoplate. (**h**) Pt /4f XPS spectra of PtBi/Pt core/shell nanoplates and commercial Pt/C.
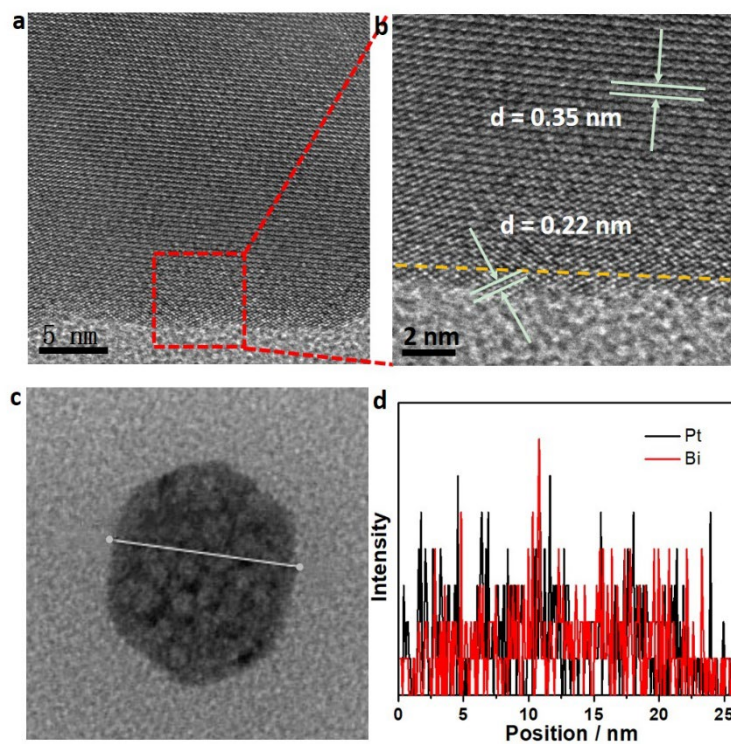
Figure 2 (**a, b**) Representative HRTEM image of as-prepared PtBi/Pt core/shell nanoplate, (**c, d**) EDX elemental line scan across single PtBi/Pt core/shell nanoplate.
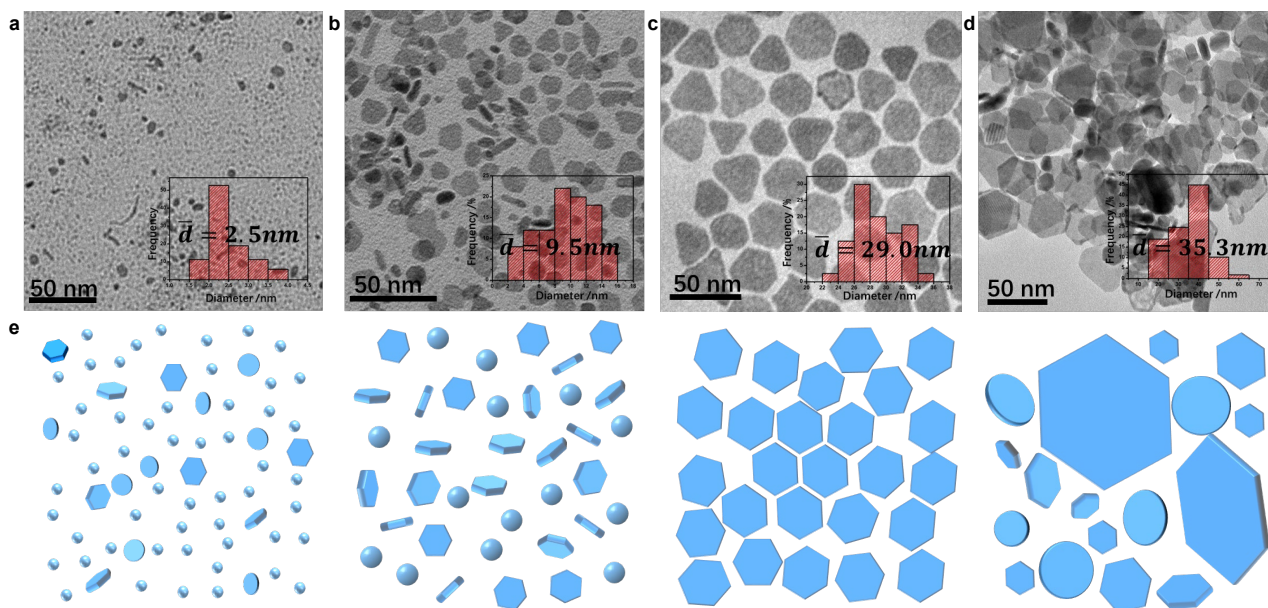
Figure 3. Structural evolution of PtBi/Pt core/shell nanoplates: (a) Representative TEM image and corresponding size distribution of products collected at 1 min, **(b)** 30 min, **(c)** 5 h, **(d)** 10 h. **(e)** Schematic illustrations of the structural evolution process of PtBi/Pt core/shell nanoplates.
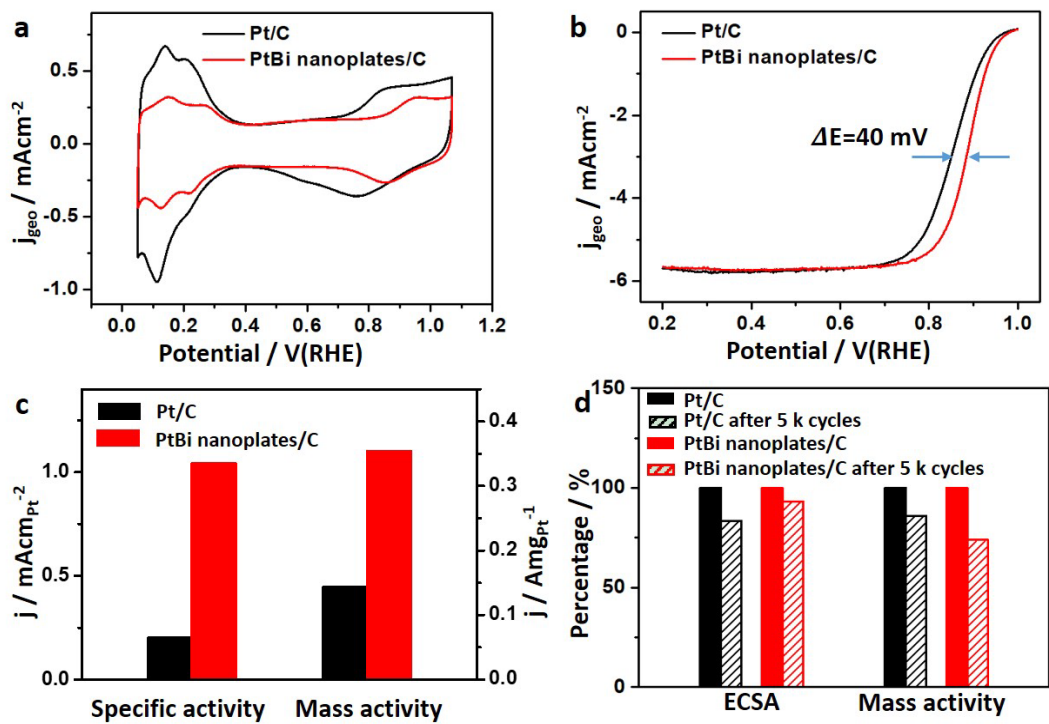
Figure 4. ORR performance. (**a**) CVs of PtBi/C and Pt/C catalysts. (**b**) ORR polarization curves of commercial Pt/C and PtBi/C catalysts. (**c**) Comparison on the specific activities and mass activities. (**d**) Comparison of ECSA and mass activity before and after 5,000 cycles.
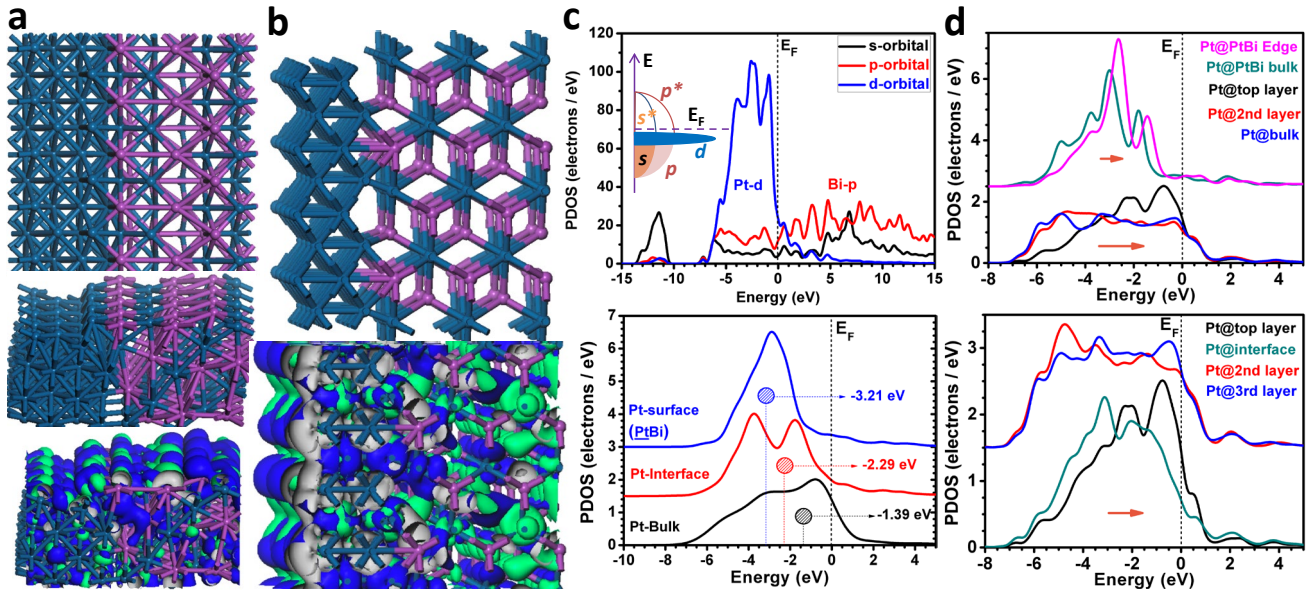
Figure 5. DFT calculations. (a) The local structure of PtBi-Pt system (top- and side-view) with bonding (blue) and anti-bonding (green) orbital contour plots (down). **(b)** The projected density of states (PDOS) of the PtBi-Pt system. **(c)** The variation of the PDOS for the Pt-5d band is shown for different regions. **(d)** The change in free energy (ΔG) profile simulates the ORR process within acidic condition and a four-electron process from the PtBi-Pt and PtBi systems respectively. **(e)** The evolutions of the local structural configurations for the simulated ORR process from the PtBi-Pt.
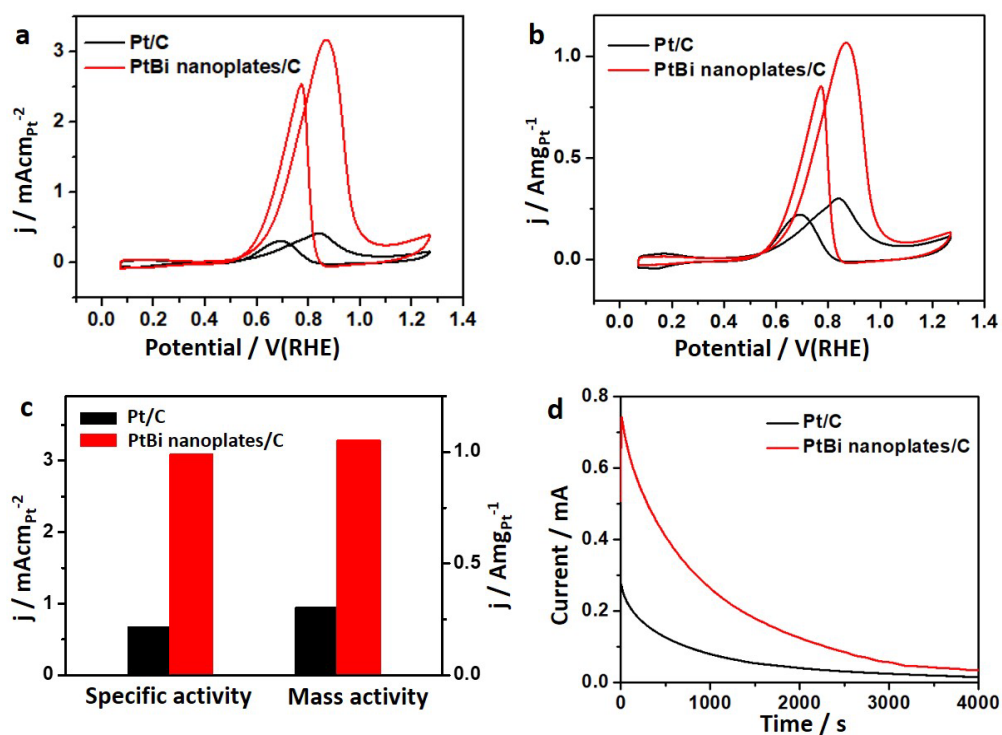
Figure 6. MOR Performance. (**a**) ECSA- and (**b**) Pt mass-normalized CVs of PtBi nanoplate/C and commercial Pt/C recorded in 0.1 M HClO₄ solution containing 0.1 M MeOH. (**c**) Histogram of specific activity and mass activity. (**d**) i-t test of PtBi nanoplate/C and commercial Pt/C in 0.1 M HClO₄ containing 0.1 M MeOH, recorded at a constant potential of 0.67 V *vs*. RHE.

For Table of Contents Only